Results in Optics 16 (2024) 100726

Contents lists available at ScienceDirect

Results in Optics

journal homepage: www.elsevier.com/locate/rio

Azimuthal Fourier decomposition for loss analysis of hollow-core tube lattice fibers, Part II: Tube thickness variation effects

Federico Melli [a], Fabio Giovanardi [b], Kostiantyn Vasko [c], Lorenzo Rosa [a], Fetah Benabid [c], Luca Vincetti [a,*]

[a] Department of Engineering "Enzo Ferrari", University of Modena and Reggio Emilia, via Vivarelli 10, Int. 1, Modena, 41125, Italy
[b] Osservatorio Astrofisico di Arcetri, INAF, Largo Enrico Fermi 5, Firenze, 50125, Italy
[c] GPPMM Group, XLIM Institute, UMR CNRS 7252, University of Limoges, Limoges, France

ARTICLE INFO

Keywords:
Hollow-core fibers
Inhibited coupling
Photonic crystal fibers
Tube lattice fibers
Coupled mode theory
Propagation loss
Geometrical deformations

ABSTRACT

The effect on confinement loss of thickness variations along the perimeter of the tubes composing the cladding of inhibited-coupling guiding Tube Lattice hollow-core fibers is investigated by using the Azimuthal Fourier Decomposition technique (developed in Part I) for the description of the cladding modal dynamics and their interaction with the fundamental core mode. The results show that the thickness inhomogeneity affects the confinement loss spectrum through confinement loss increase and frequency red- and blue-shift of the high-loss spectral regions. The magnitudes of the confinement loss increase and the high-loss region frequency shift strongly depend on the spatial distribution of the thickness inhomogeneity. The study provides insight into the loss mechanism of non-ideal tube lattice fibers, it allows to quantify the impact of such kind of structural deformations, identifying the route to make fibers more resilient to such fabrication imperfections, and highlighting once again the importance played in inhibited-coupling fibers by the interaction between core modes and the intricate set of cladding modes.

1. Introduction

Hollow-Core Photonic Crystal Fibers (HCPCFs) based on the Inhibited Coupling (IC) waveguiding mechanism exhibit very attractive properties such as wide transmission bandwidth, low loss, low dispersion, and a relatively simple cladding structure. In the last few years, IC guiding HCPCFs (IC-HCPCF)s with Tube Lattice cladding (TLFs) have experienced an impressive transmission loss reduction (Debord et al., 2017; Pryamikov et al., 2011; Sakr et al., 2019; Gao et al., 2019; Amrani et al., 2021). However, a gap remains between the experimentally measured loss and the theoretically achievable minimum defined by confinement loss (CL) (Melli et al., 2021; Joseph Weiblen et al., 2016). This difference is currently attributed to the non-ideal structure of real fibers, such as glass surface roughness due to frozen-in thermal surface capillary waves (SCW) excited during the fiber drawing process (Roberts et al., 2005), deformations of the fiber cross section (Joseph Weiblen et al., 2016), and micro- bending loss (Sakr et al., 2020). Furthermore, these fibers are commonly fabricated using the 'stack and draw' technique (Knight et al., 1996), supplemented by pressurizing the core and cladding holes (Benabid and Roberts, 2011) to control both the hole size and the silica thickness. Due to variations in local surface tension between cladding regions with and without nodes, the thickness of the glass surrounding a fiber hole is not necessarily uniform along its perimeter. Studies on the tolerances of some deformations has been carried out (Joseph Weiblen et al., 2016), however, a thorough theoretical analysis showing in detail the causes of this gap and the role of the thickness inhomogeneity in altering CL values and spectral structure is not yet available. These considerations bear importance both for the physics of light guidance via the IC mechanism and in several applications, especially those related to IC-HCPCF designs or new manufacturing processes. The current effort in designing ultra-low loss IC-HCPCF in the short wavelength range faces a limit in the CL defined by surface roughness, regardless of the confinement power of the cladding design (Osório et al., 2019). In the context of fiber manufacturing, new processes were recently proposed in literature for both infrared (Ventura et al., 2020; Carcreff et al., 2021) and THz (Cruz et al., 2017) ranges. They offer more flexibility in terms of transverse geometry configuration, but do not yet guarantee the same accuracy and repeatability of the more traditional stack-and-draw approach (Debord et al., 2019). Finally, in more and more applications, an additional layer is added on the inner wall of HC-PCF for fiber functionalization (Shi et al., 2008; Barozzi et al., 2017) and bio-detection (Khozeymeh et al., 2022) or for reducing or controlling

* Corresponding author.
E-mail addresses: fetah.benabid@unilim.fr (F. Benabid), luca.vincetti@unimore.it (L. Vincetti).

https://doi.org/10.1016/j.rio.2024.100726
Received 11 March 2024; Received in revised form 13 June 2024; Accepted 16 July 2024
Available online 20 July 2024

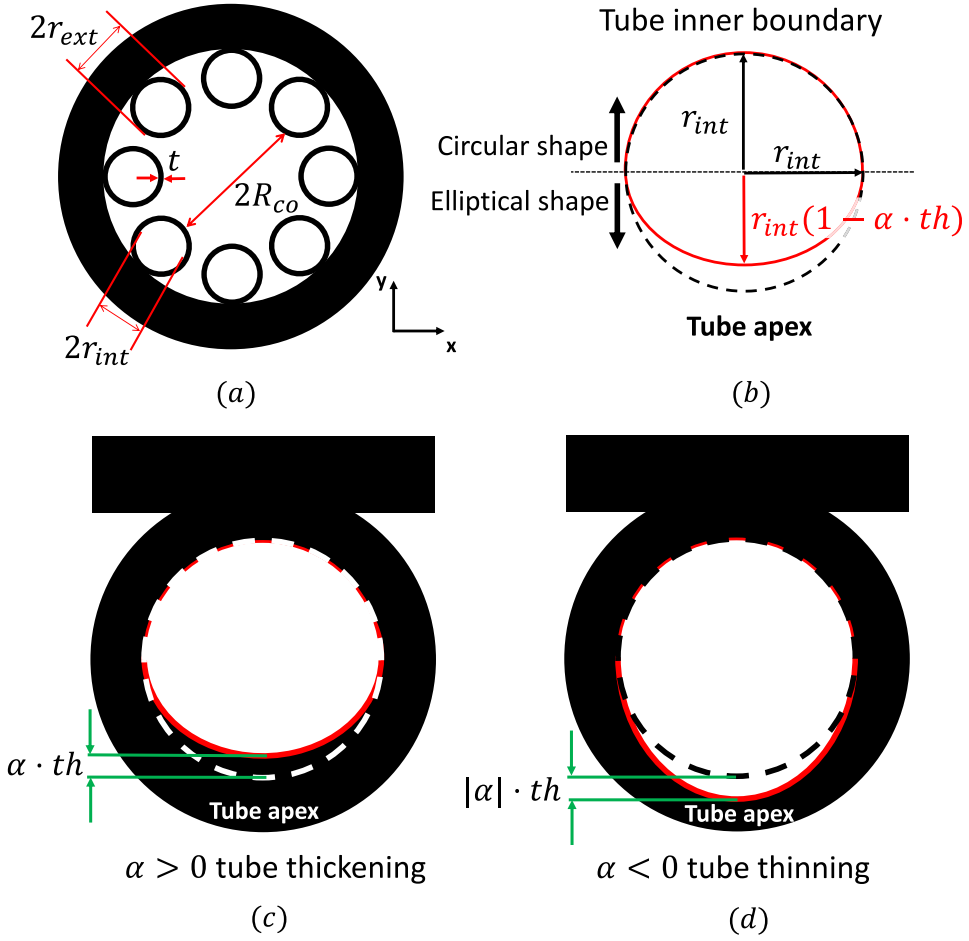

Fig. 1. (a) Example of cross-section of the analyzed fibers together with the geometrical parameters. (b) Shape of the inner boundary of a deformed tube (red solid line) and of an ideal one (black dashed line). (c) Magnified tube highlighting the thickening variation ($\alpha > 0$). (d) Magnified tube highlighting the thinning variation ($\alpha < 0$). (For interpretation of the references to color in this figure legend, the reader is referred to the web version of this article.)

atom-surface interaction in all-fiber alkali-vapor photonic microcells (PMCs) (Bradley et al., 2014; Zheng, 2017). Here, the thickness of this layer can be locally altered due to the deposition process or bio-detection causing a distortion of the real cross section with respect to the ideal one. In this work, we exploit the Azimuthal Fourier Decomposition (AFD) technique (developed in Part I Melli et al., 2024) to evaluate the impact of transverse geometrical imperfections in the cladding tube thickness and, more accurately, when the thickness changes along the tube perimeter. The analysis shows that local thickness variations induce changes in both the cut-off frequencies and electric field distribution of the fiber cladding modes (CLMs), causing alteration of the CL magnitude and spectral structure. In particular, AFD clearly and effectively shows that the spatial field distribution change is responsible for the coupling enhancement between the Fundamental Mode (FM) and CLMs which are uncoupled in ideal fibers, and why this occurs only for particular classes of CLMs and thickness variations. Finally, guidelines for designing more robust TLFs against tube thickness variations are given.

2. Analysis

Fig. 1 shows the cross-section of a TLF and summarizes the type of transverse structural perturbation here investigated. Fig. 1(a) highlights the physical and geometrical parameters: R_{co} is the TLF hollow core radius, r_{ext} and r_{int} are the outer and inner radius, respectively, of the cladding tubes with thickness t and refractive index n_d. Unlike an ideal fiber, the tube thickness t is azimuthally varying over the inner half of the cladding tubes' circumferences. It progressively increases or decreases when approaching the extremity of the tube inner boundary with the fiber hollow core, that we label hereinafter "tube apex". Fig. 1(b) shows the radial parameters of the deformed tube. The outer half of the tube, facing the tube bonding point with the external dielectric wall, can be considered as belonging to a circular tube with inner radius r_{int}, whereas the inner half belongs to an elliptical shape with semi-axes equal to r_{int} and $r_{int} - \alpha \cdot t$, respectively. α is the normalized thickening parameter, and $\Delta t = \alpha \cdot t$ is the maximum thickness variation reached at the tube apex with respect to the ideal structure, which is defined as $\alpha = 0$. Fig. 1(c) and (d) show schematically the cases of tube apex thickening (i.e. $\alpha > 0$) and thinning (i.e. $\alpha < 0$), respectively.

In order to better highlight the effects of the perturbations, we introduce the normalized frequency F:

$$F = \frac{2t}{\lambda}\sqrt{n_d^2 - 1}, \tag{1}$$

and express CL via the normalized confinement loss NCL (Vincetti, 2016):

$$NCL = \frac{CL}{CL_{min}},$$

where

$$CL_{min} = 5 \cdot 10^{-4} \frac{\lambda^{4.5}}{R_{co}^4} \left(1 - \frac{t}{r_{ext}}\right)^{-12} \frac{\sqrt{n_d^2 - 1}}{t\sqrt{r_{ext}}} e^{\frac{2\lambda}{r_{ext}(n_d^2 - 1)}}.$$

This allows to abstract the dependence on wavelength, core size, tube thickness, and dielectric refractive index, which is present even in the ideal fibers.

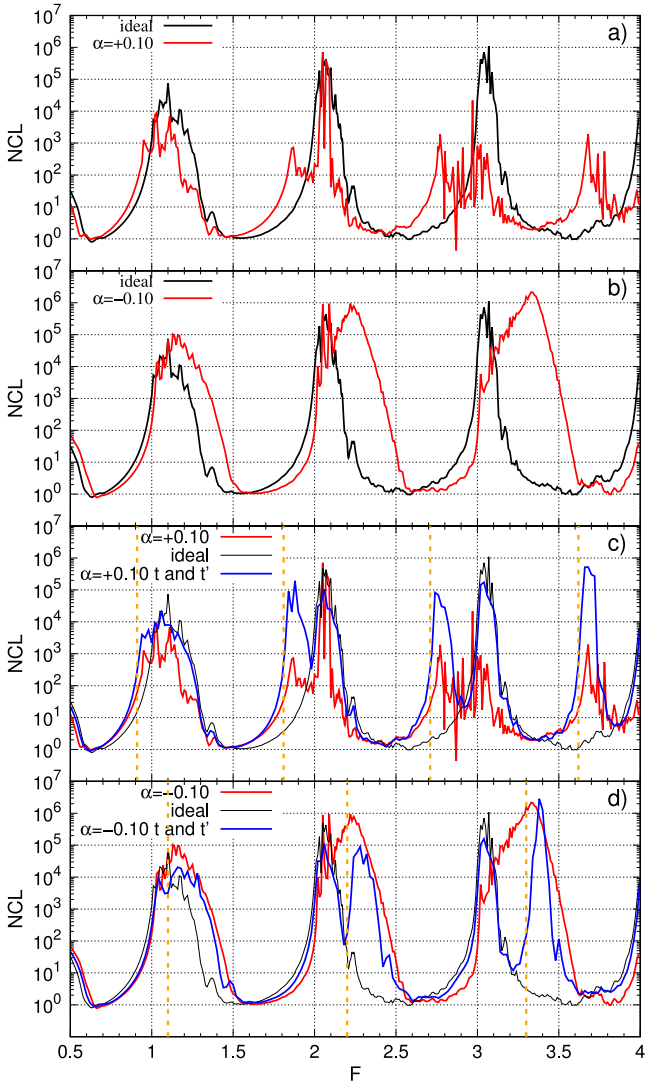

Fig. 2. NCL spectra of an 8-tube TLF (#1) for (a) tube thickening with $\alpha = 0.1$, (b) thinning with $\alpha = -0.1$, and their comparison with a TLF with tubes having azimuthally constant thickness alternately of t and (c) $t' = t + 0.1t$ or (d) $t' = t - 0.1t$. (For interpretation of the references to color in this figure legend, the reader is referred to the web version of this article.)

Fig. 2 shows the NCL spectra of an 8-tube TLF, hereinafter called Fiber#1, over a frequency range of $F = 0.5 \div 4.0$, comprising thus four transmission bands (TBs): the fundamental TB (i.e. $F = 0.5 \div 1.0$) and the first three higher-order TBs. The geometrical and material parameters are reported in the first row of Table 1. Fiber#1 has an overlap between the tubes and the external silica wall at the bonding point equal to $t/50$ the same as all the other fibers here analyzed. Fig. 2(a) and (b) compare the NCL of an ideal fiber (black curves) with fibers exhibiting tube apex thickening ($\alpha = 0.1$, solid red curve) and thinning (i.e. $\alpha = -0.1$, dashed red curve), respectively. Here, the impact of the thickness variation mainly affects the High-Loss Regions (HLRs) of NCL, whereas the values of the minima in the TBs are basically unchanged. We recall that the HLRs correspond to spectral ranges where the fundamental core mode (FM) and CLMs are phase-matched both longitudinally and transversely (Couny et al., 2007; Debord et al., 2019), and hence there is a strong coupling between the core mode and the cladding ones. This occurs around $F = i$, where i is a positive integer. Consequently, and due just to the dependence of F on thickness, positive α (thickening) induces HLRs to shift toward lower frequencies (red-shift), and negative values of α (thinning) induce HLR blue-shift. Also, this F-thickness dependence explains the observed increase of the magnitude of the shift as the TB order increases. However, the loss spectra changing cannot be ascribed only to the cutoff frequency shift due to thickening and the thinning of the tube apex. In fact, as it is deeply described in the next sections also the field profiles of CLMs will be affected upon tube thickness variation. In order to illustrate this point, we consider Fiber#1, but with a cladding comprised of alternating ideal tubes having thicknesses of t and $t' = \alpha \cdot t$ respectively. Fig. 2(c) and (d) show the spectra obtained with this modified Fiber#1 (blue curves) along with the ideal fiber (black curves) and the one having either thinned or thickened tubes with $\alpha = \pm 0.1$ (red curves). Even though both types of perturbations cause HLR broadening and frequency-shift, the results show very different HLR spectral structures, thus indicating that the mechanism cannot be solely reduced to a thickness-variation-induced frequency-shift. As a matter of fact, the above examples show the importance of knowing the nature of CLMs and how they evolve under structural perturbations. Indeed, while the case of fibers with alternating tubes is easily understood through the contribution of the two ideally circular tubes with two different thicknesses to the modal content of the cladding (Kharadly and Lewis, 1969; Debord et al., 2015; Melli et al., 2024), the case of fibers with identical distorted thickness requires a prior knowledge of the modal content of these non-ideal circular cladding single tubes. This is illustrated in Fig. 2(c) and (d) by vertical dashed orange lines, which mark the integer values of $F' = 2t'/\lambda\sqrt{(n^2-1)}$. Here, HLRs are split in two subsets with the same shape and bandwidth, one corresponding to integer values of F, and the other to integer values of F'. However, in the case of non-azimuthally uniform tube thickness variation, the spectral shapes are different from the above one, and stand out with their HLR's strong dependence on the sign of α, i.e. tube thickening impacts the CL spectrum differently from tube thinning. In case of thickening ($\alpha > 0$), there is a red broadening of the HLRs with the appearance of isolated peaks in the red edges with lower amplitudes than the original HLRs. In case of thinning ($\alpha < 0$), there is a HLRs blue shift without the appearance of peaks or HLRs splitting and with a stronger shift for the blue HLR edges than the red ones.

Fig. 3 extends the above calculations to several different values of α. The results indicate four regimes depending on the α value. The first regime corresponds to small positive α shown in Fig. 3(a). Here, the NCL minimum value and frequency location are not affected, and the NCL spectrum change is limited to a red-shift of the HLRs. The second regime corresponds to larger thickening (see Fig. 3(b)) where the HLRs break down into several structured and resolved narrow peaks, causing a serious degradation of the TBs and an increase of the minimum NCL. We note that the values of α corresponding to the transition from one regime to the other depend on the TB order. The fundamental band is more resilient and significant effects occur only for thickenings greater than 20% of the tube thickness. Considering the fourth band, relative thickenings of 5% and larger are enough to affect the TB, which is completely compromised for a relative thickening of 20%. Finally, for perturbations having 50% relative thickening, all TBs are seriously degraded. The third regime corresponds to small tube thinning (Fig. 3(c)). Here, HLRs broaden with strong blue shifts of the blue-edges, TBs shrink, but without variation of the NCL minimum. With larger thinning (Fig. 3(d)) we have the fourth regime. Here, the HLRs tend to occupy all the TBs, which disappear. Also in this case, the entity of the perturbation defining the transition from one regime to the other depends on the order of the TB, where the low order ones are more robust than the higher order ones. In order to investigate the impact of the thickness perturbation on the modal confinement the effective area A_{eff} (Rosa et al., 2021) of the perturbed and ideal fibers have been compared. Fig. 4 shows the relative variation of the effective area $\Delta A_{eff}\%$:

$$\Delta A_{eff}\% = \frac{A_{eff_{perturbed}} - A_{eff_{ideal}}}{A_{eff_{ideal}}} \cdot 100, \tag{2}$$

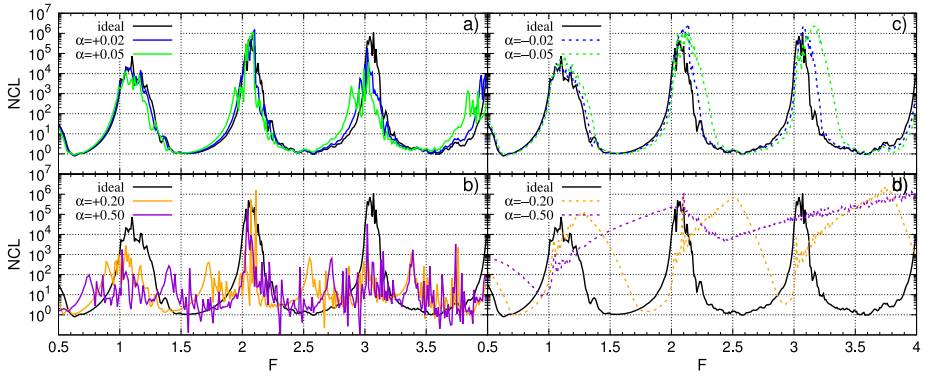

Fig. 3. NCL spectra of an 8-tube TLF (#1) in the frequency range [0.5 – 4.0] for different (a) positive $\alpha = +0.02, +0.05$, (b) $\alpha = +0.20, +0.50$, and (c) negative $\alpha = -0.02, -0.05$, (d) $\alpha = -0.20, -0.50$ thickness variations. (For interpretation of the references to color in this figure legend, the reader is referred to the web version of this article.)

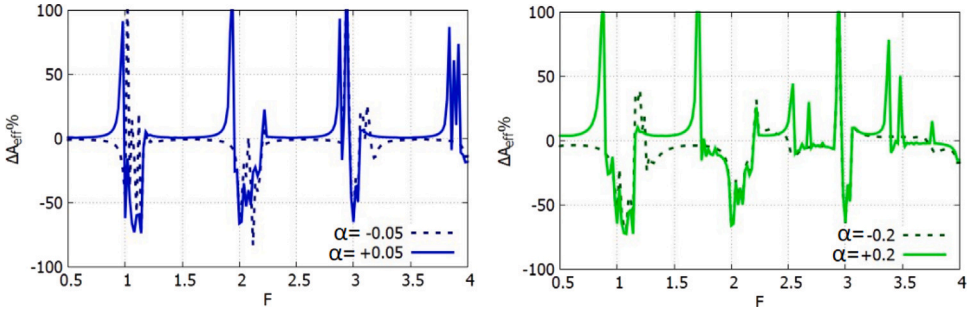

Fig. 4. Relative effective area variation with $\alpha = \pm 0.05$ (left) and $\alpha = \pm 0.2$ (right) for fiber #1.

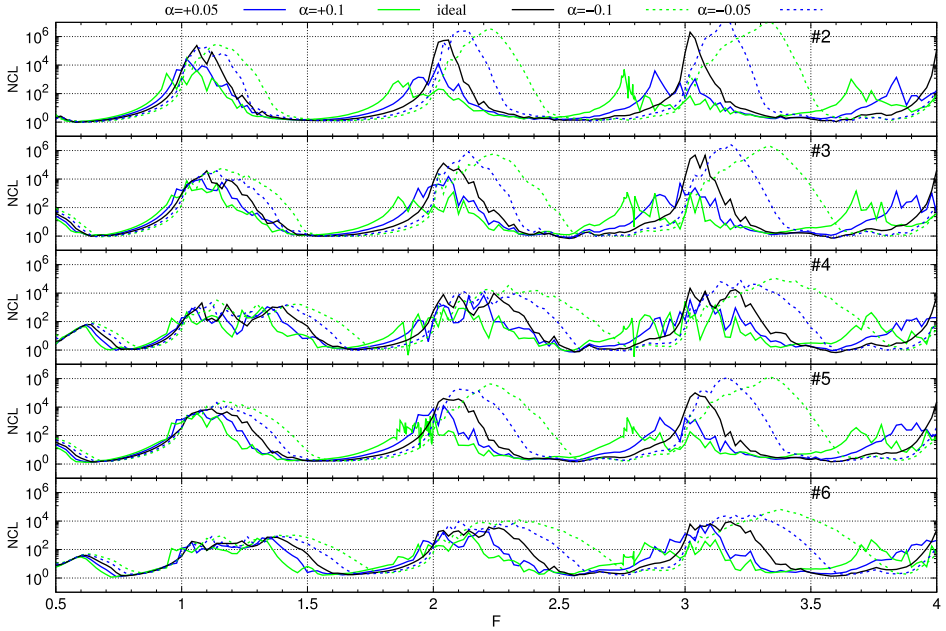

Fig. 5. NCL spectra of TLFs from #2 to #6, whose design parameters are reported in Table 1, for different positive (solid lines) and negative (dashed lines) values of the thickness parameter: $\alpha = \pm 0.05, \pm 0.1$.

of the FM of fiber#1 in the four regimes above defined. In case of small perturbations ($\Delta\alpha = \pm 0.05$) A_{eff} is affected close to the blue and red edges of HLRs. In the TBs centers the impact is very small. In case of strong perturbations ($\Delta\alpha = \pm 0.2$) also the TBs are affected, with resolved narrow peaks in case of tube thickening.

The above analysis has been carried out on different TLFs listed in Table 1, which is constructed in such a way that a minimum number of parameters (among t, n_d, r_{ext}, and N) is changed between two adjacent fibers. Last column of Table 1 reports the values of $\rho = 1 - t/r_{ext}$ parameter. The importance of the role played by this parameter will be highlighted in the next sections, and in particular in Fig. 14. The FM CL spectra of eleven TLFs having different geometrical parameters, different number of tubes N, and different refractive index n_d of the dielectric were calculated for different α. We considered fibers with 8 and 6 tubes since these are the most widely used structures. The results show that all the TLFs exhibited the same trends as the ones

Table 1
TLF parameters. All geometrical parameters are given in micrometers.

Fiber	t	r_{ext}	n_d	N	R_{co}	ρ
#1	0.75	6.0	1.45	8	13.6	0.875
#2	0.75	10.0	1.45	8	20.0	0.925
#3	1.25	10.0	1.45	8	20.0	0.875
#4	1.25	10.0	2.45	8	20.0	0.875
#5	1.25	10.0	1.45	6	13.6	0.875
#6	1.25	10.0	2.45	6	13.6	0.875
#7	0.75	10.0	2.45	8	20.0	0.925
#8	0.6	6	1.45	8	13.6	0.9
#9	0.6	6	2.45	8	13.6	0.9
#10	0.5	12	2.45	8	22	0.958
#11	0.5	12	1.45	8	22	0.958

discussed above. Fig. 5 illustrates this by comparing the NCL spectra for $\alpha = \pm 0.05, \pm 0.1$ and for six TLFs (fibers from #1 to #6). The spectra readily exhibit the same trends as those of Fig. 3, demonstrated by the HLR's small frequency red-shifted resolved narrow peaks in the case of tube thickening, and by the HLR's strong blue-shift in the case of tube thinning.

Finding out the physical mechanisms behind the alteration of the CL spectra here discussed entails analyzing the CLMs' evolution from that of ideal fiber due to the tube structural perturbation, and subsequent FM-CLMs coupling modification. In the next section, we use the single tube approximation and the Azimuthal Fourier Decomposition (AFD) (Melli et al., 2024) to analyze and interpret the above results.

3. Model

In IC fibers, the HLRs and TBs are defined by the coupling between the FM and CLMs with slow and quick electric field spatial variations (Couny et al., 2007), corresponding to high and low values of the overlap integral:

$$K = \iint_{S_\infty} \overline{E}_{t_{co}} \cdot \overline{E}_{t_{cl}} \, dS \tag{3}$$

respectively. S_∞ is the whole fiber cross-section, $\overline{E}_{t_{co}}$ and $\overline{E}_{t_{cl}}$ are the electric field transverse components of the FM and CLM, respectively. Since the FM effective index $n_{eff_{FM}}$ is close to but lower than 1, the frequencies where couplings occur can be approximated by the CLM cut-off frequencies F_c (Debord et al., 2019; Melli et al., 2024). Moreover, in TLFs the large pitch regime allows to apply the single-tube approximation and CLMs can be described in terms of superposition of identical modes of an isolated single tube (Vincetti and Rosa, 2019). In the following, we will refer to the modes confined in the dielectric of an isolated tube as CLMs (Melli et al., 2024). These modes are classified by an azimuthal index μ defining the number of periods of the electric field distribution along the azimuthal direction, a radial index ν defining the number of maxima and minima along the radial direction, and two different polarizations $HE_{\mu,\nu}$ and $EH_{\mu,\nu}$ where the electric field dominant component is the azimuthal and radial one, respectively (Kharadly and Lewis, 1969; Vincetti and Setti, 2010). Summing up, in TLFs, HLRs and TBs are defined by the spectral distribution of the cut-off frequencies of the CLMs with slow and high azimuthal index, respectively (Melli et al., 2024). In the fiber here investigated, the azimuthal change of tube thickness modifies both the cut-off and electric field distribution of the CLMs, and in turn the CL spectra. Fig. 6 immediately gives an idea of the impact of tube thickness variation on those. It shows the evolution of the dispersion curve and the electric field distribution of representative modes among low azimuthal index CLMs (here $HE_{2,3}$) and among high azimuthal index ones ($HE_{10,3}$) of Fiber#1 versus the thickening parameter α of an isolated tube having a varying thickness as shown in Fig. 1. The results readily show that the change in α sign and value affects both the tube mode dispersion (and thus the cut-off frequencies F_c) and the field profile.

The effect on the cut-off frequency is quantified in Fig. 7, where the variation $\Delta F_c = F_c - F_{c_0}$ with respect to the value F_{c_0} of the ideal tube is shown versus the normalized thickening parameter α, for different CLMs with different azimuthal (Fig. 7(a)) and radial (Fig. 7(b)) indices. Fig. 7(a) shows different kinds of dependence according to the sign of α. The frequency shift is positive with a weak dependence proportional to the azimuthal index μ in case of thinning and it is negative with a stronger dependence inversely proportional to μ in case of thickening. Fig. 7(b) analyzes the radial index dependence. Again, there is a stronger dependence in case of thickening than of thinning, but the dependence on the radial index is opposite with respect to the azimuthal one: in case of thinning there is an inverse dependence on ν, whereas in case of thickening the dependence is direct.

In order to investigate the consequences of the electric field profile change induced by the thickness variation, we apply the AFD technique (Melli et al., 2024). The CLM-FM coupling can be estimated by considering the Azimuthal Spectral Overlap (ASO) coefficient g:

$$g(r) = \sum_{s=r,\theta} \left(\sum_{m=-\infty}^{m=\infty} R_m^{co_s}(r) R_{-m}^{cl_s}(r) \right) \tag{4}$$

where

$$R_m^{(co/cl)_s}(r) = \frac{1}{2\pi} \int_0^{2\pi} E_{(co/cl)_s}(r,\theta) e^{-jm\theta} d\theta$$

is the azimuthal Fourier coefficient of the azimuthal Fourier series:

$$E_{co_s} = \sum_{m=-\infty}^{+\infty} R_m^{co_s}(r_{int}) e^{jm\theta}, \quad E_{cl_s} = \sum_{m=-\infty}^{+\infty} R_m^{cl_s}(r_{int}) e^{jm\theta}.$$

Since the coupling strength between two modes is proportional to the overlap of the corresponding azimuthal spectra, and the loss due to the coupling is proportional to $|g^2|$, in the following we analyze how the tube variations affect the azimuthal spectra and consequently the ASO. Moreover, spectra show an Hermitian symmetry (Melli et al., 2024) thus for shake of simplicity in the following only single side spectra representation is used.

Fig. 8 analyzes profiles and corresponding azimuthal spectra of the radial and azimuthal components of the FM y-polarized electric field on the tube highlighted in the figure. Results not shown here for sake of brevity, obtained by thinning and thickening the tubes, show the FM spectra are not appreciably affected by thickness tube variations. For the following analysis, the most important feature is that the azimuthal spectra are dominantly populated at low azimuthal frequencies, showing a "low pass-like" profile.

Fig. 9(a) investigates the effect of tube thinning on the CLMs azimuthal spectra. Only EH CLMs are here reported for sake of brevity, since the effects on HE CLMs are very similar. Since EH CLMs are radially polarized (Vincetti and Setti, 2010; Kharadly and Lewis, 1969), the azimuthal spectra of the azimuthal component is negligible with respect to the radial one, so in Fig. 9(a) only $|R_m^{cl_r}|$ are shown. The azimuthal spectra of CLMs calculated at the inner and outer boundaries do not show significant differences. In order to clearly highlight the ASO between CLM and FM spectra, the figures are filled with a gray colored background, whose darkness is scaled according to the amplitude of the dominant component coefficients $R_m^{co_r}$ of the y-polarized FM calculated on the inner boundary of the tube highlighted in Fig. 8. Consequently, the FM-CLMs coupling can be visually assessed by the overlap between the orange drop-lines and the background's darkest region and quantified by the g parameter plotted in Fig. 9(b). For ideal tubes, the $R_m^{cl_r}$ CLM azimuthal spectra feature a dominant spectral component centered at the azimuthal index of the tube mode ($m = \mu$). Also, the results show that, among the CLMs here shown, only the $EH_{5,3}$ exhibits an overlap with the FM, resulting in high ASO coefficients and consequently contributing to the HLRs. Conversely, the dominant spectral component of higher azimuthal index CLMs falls where the FM spectrum is negligible. According to IC model, their ASO and their contribution to CL is expected to be low. This is readily shown

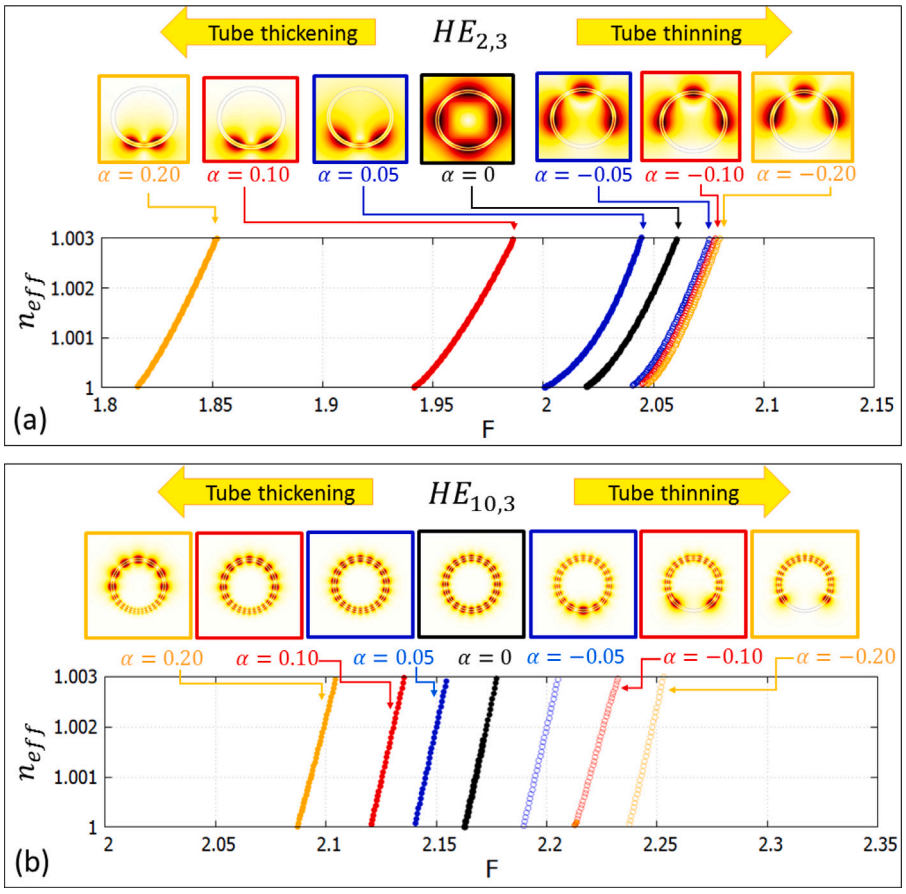

Fig. 6. Evolution of the field distribution (top) and dispersion curve (bottom) of the single tube cladding modes (a) $HE_{2,3}$ and (b) $HE_{10,3}$, for different values of the parameter α. The tube parameters are those of #1. (For interpretation of the references to color in this figure legend, the reader is referred to the web version of this article.)

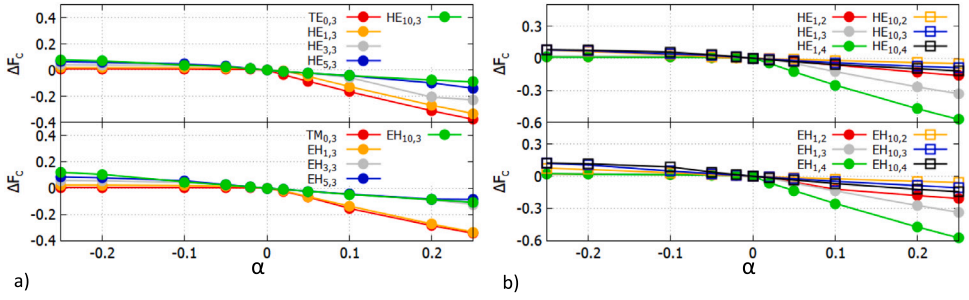

Fig. 7. Cut-off frequency variation ΔF_c vs α for a number of CLMs of varying (a) azimuthal index and (b) radial index. Tube parameters are those of Fiber#1.

by the values of the g parameter computed on the inner boundary ($r = r_{ini}$) shown in Fig. 9(b). ASO g value for $EH_{5,3}$ is close to 20-fold higher than those for $EH_{10,3}, EH_{16,3}, EH_{25,3}$ (see Fig. 9(b)).

As shown in Fig. 6, when tube thinning is applied, the field distributions, and in particular the azimuthal dependence, change causing a broadening of the CLM spectra on both sides. The broadening increases with stronger thinning. In particular, the broadening toward low m values contributes to increase the ASO. The broadening depends very weakly on the CLM azimuthal index number. Consequently, the overlap between the CLM and FM spectra is stronger for lower azimuthal index CLMs. For example, with $\alpha = -0.05$, not only CLMs with azimuthal index $\mu = 5$, but also CLMs with $\mu = 10$ have the left side of the azimuthal spectra (orange lines) overlapped with the FM one (dark background). Despite the spectral broadening, CLMs with $\mu = 16$ and $\mu = 25$ still have a negligible overlap with the FM spectrum. By increasing the thinning ($\alpha = -0.1$) the wider broadening causes a non-negligible overlap also for mode with $\mu = 16$, while CLMs with $\mu = 25$ still have a negligible overlap. The dynamic is clearly shown by the α dependence of g. For $\alpha = -0.05$, g increases only for CLMs with $\mu = 5, 10$ (orange and green curve of Fig. 9(b)), whereas it is almost unchanged for CLMs with higher azimuthal index. By increasing the thinning to $\alpha = -0.1$, g increases also for CLMs with $\mu = 16$. A spreading of the azimuthal spectra is also observed in case of tube thickening, as shown in Fig. 10 for the case of $HE_{10,3}$, and $EH_{10,3}$ CLMs. Unlike the tube thinning case, it can be observed that thickening causes a smaller broadening of the CLMs spectra, and the g parameter changes little. Finally, Fig. 11, compares the spectra and ASO of EH CLMs with same azimuthal index ($\mu = 16$) and different radial index, and thus with F_c falling in different TBs. Results clearly show the spreading caused by the thinning and the corresponding ASO increase with the CLM radial index.

In conclusion, the tube thickness variation causes two changes in the CLMs features. The first is a change in the CLMs cut-off frequencies, which is stronger in case of tube thickening and for low azimuthal index

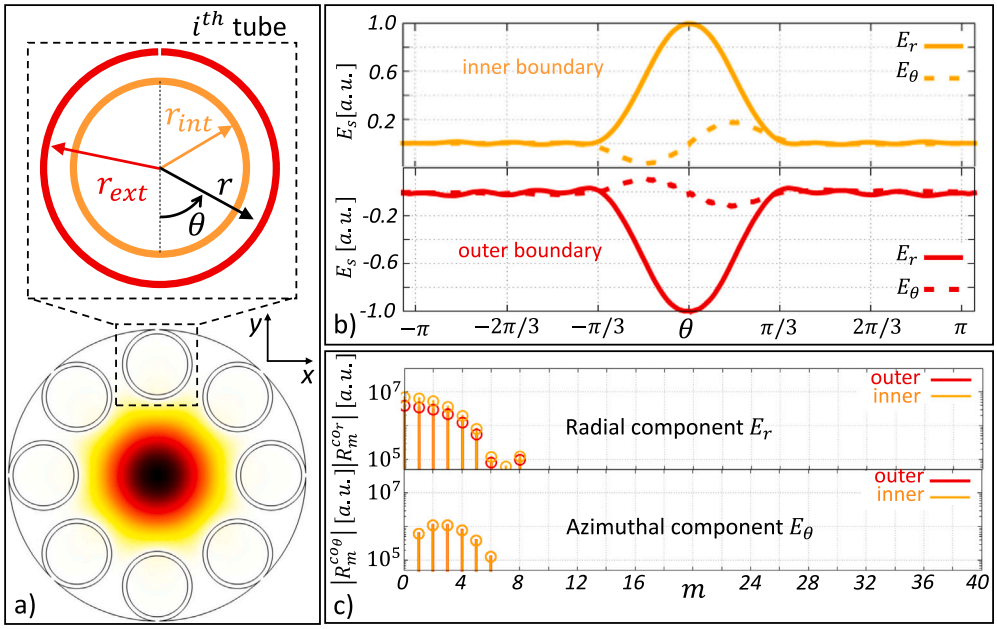

Fig. 8. (a) Fiber#1 cross section with FM field distribution and detail of local frame of reference, and inner and outer boundary of the ith tube. (b) Radial (solid line) and azimuthal (dashed line) y-polarized FM electric field components along the inner (orange) and outer (red) boundaries. (c) $|R_m^{co_r}|$ (top) and $|R_m^{co_\theta}|$ (bottom) coefficients of the profiles plotted in (b). (For interpretation of the references to color in this figure legend, the reader is referred to the web version of this article.)

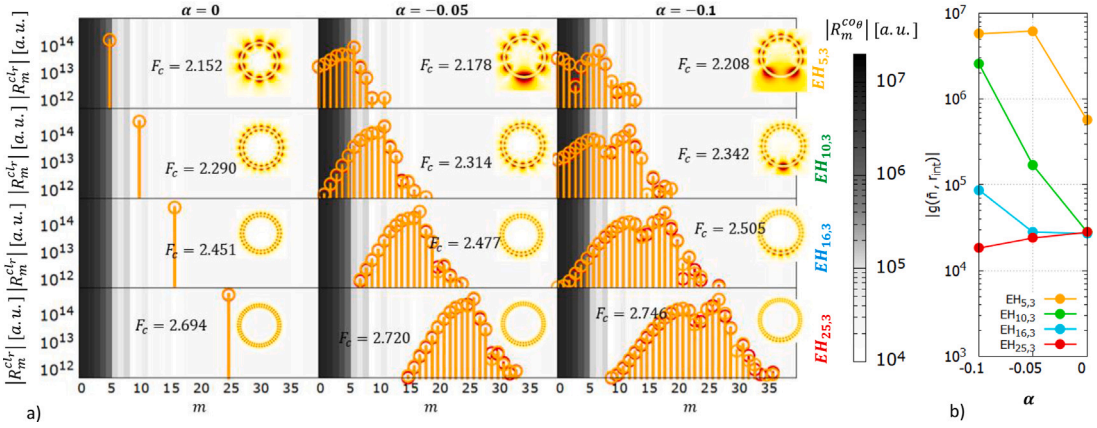

Fig. 9. EH CLMs azimuthal spectra, in case of tube thinning. Left panel (a): spectra of $|R_m^{cl_r}|$ calculated at the inner (orange) and outer (red) boundary of tube ith of Fiber#1 highlighted in Fig. 8 for four different modes (from top to bottom: $EH_{5,3}$, $EH_{10,3}$, $EH_{16,3}$, $EH_{25,3}$) and different perturbations (ideal tube on left side, $\alpha = -0.05$ at center, and $\alpha = 0.10$ on right side). Background gray scale shows the corresponding value of $|R_{m,o_r}|$. Insets show the field distribution of the modes. Cut-off frequency is also shown. Right panel (b): magnitude of the ASO coefficient g calculated along the inner boundary ($r = r_{int}$) for all modes shown in the left panel (a). (For interpretation of the references to color in this figure legend, the reader is referred to the web version of this article.)

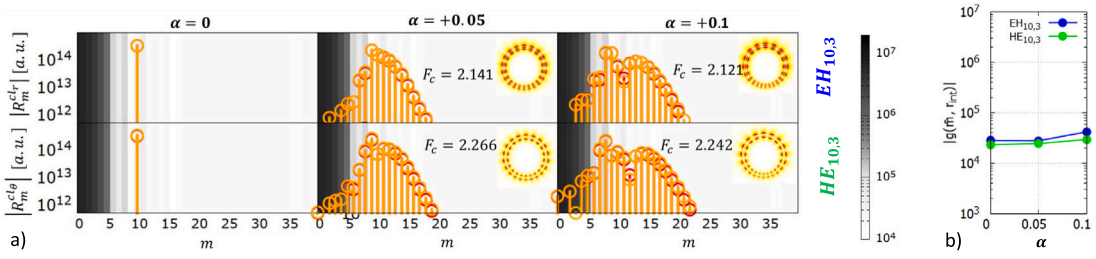

Fig. 10. CLM spectra, in case of tube thickening. Left panel (a): spectra of $|R_m^{cl_\theta}|$ and $|R_m^{cl_r}|$ calculated at the inner (orange) and outer (red) boundary of tube 1 of Fiber#1 for two different CLMs having the same indexes ($EH_{10,3}$ at the top and $HE_{10,3}$ at the bottom) and different perturbations (ideal tube on left side, $\alpha = \pm 0.05$ at center, and $\alpha = \pm 0.10$ on right side). Background gray scale shows the corresponding value of $|R_{m,o_r}|$. Insets show the field distribution of the modes. Cut-off frequency is also shown. Right panel (b): magnitude of the ASO coefficient g computed along the inner boundary ($r = r_{int}$) for all modes shown in the left panel (a). (For interpretation of the references to color in this figure legend, the reader is referred to the web version of this article.)

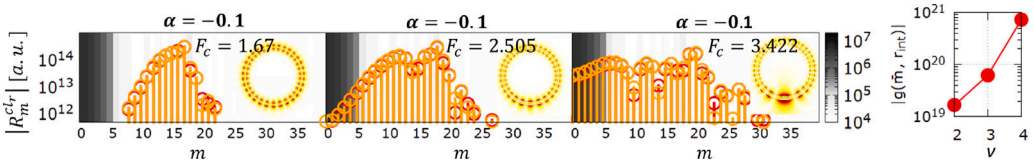

Fig. 11. $EH_{16,\nu}$ CLM spectra, in case of tube thickening ($\alpha = -0.1$), for different radial index ν. Left panel (a): spectra of $|R_m^{cl_r}|$ computed at the inner (orange) and outer (red) boundary of tube 1 of Fiber#1 of the CLMs $EH_{16,\nu}$ with different radial index: $\nu = 2$ (left), $\nu = 3$ (center), $\nu = 4$ (right). Background gray scale shows the corresponding value of $|R_m^{co_r}|$. Insets show the field distribution of the modes. Cut-off frequency is also shown. Right panel (b): magnitude of the ASO coefficient g computed along the inner boundary ($r = r_{int}$) for all modes shown in the left panel (a). (For interpretation of the references to color in this figure legend, the reader is referred to the web version of this article.)

CLMs. This explains the additional peaks appearing in case of tube thickening in Figs. 2, 3, and 5, causing the red shift of the HLRs red-edges. In case of tube thinning, cut-offs are weakly affected and do not play a significant role in loss enhancement. The second is the change in the spatial distribution and thus in the coupling strength quantified by the ASO coefficient g. In this case, the impact of thickening and thinning reverses. In case of thickening, the spatial deformation causes a weak effect of the coupling strength. Conversely, tube thinning significantly modifies the ASO causing an enhancement of the coupling, and of the consequent loss of the FM due to CLMs which are only negligibly coupled in the ideal fiber. This explains the blue shift of the HLRs blue-edges. Red-edges are not affected because they are defined by low azimuthal index CLMs, whose ASO is already high and thus not particularly affected by the thinning. The little blue-shift is mainly due to the weak change of their cut-off frequencies. Both the F_c frequency shift and the azimuthal spectrum broadening increase with the radial index, and thus with the order of the TB.

4. Model validation

In order to verify the validity of the proposed approach, we focused on the third TB of Fiber#1 in case of $\alpha = \pm 0.10$. Fig. 12 compares the loss, the real and imaginary parts of Fiber#1's FM field distribution at particular frequencies ($F_\alpha = 2.770$, $F_\beta = 2.798$, $F_\gamma = 2.208$, $F_\delta = 2.342$) highlighted with vertical dotted lines. In case of $\alpha = +0.1$, Fig. 12(a) compares points 1 and 2 at $F_\alpha = 2.770$, showing that the loss in the perturbed fiber is 250-fold the ideal one. The inspection of the corresponding fields labeled 2 in the blue box of Fig. 12(c) shows FM hybridizes with a slow azimuthal varying CLM having only one peak in case of perturbation. Details of the hybridization are highlighted in the inset. The hybridization is completely absent in the ideal fiber, labeled 1, according to the model, since at this normalized frequency no CLMs with non-negligible ASO exist. The same comments can be made about the loss and fields corresponding to points 3 and 4 at $F_\beta = 2.798$, except in this case the slow varying CLM has two lobes (green inset). Mode profiles and peak frequencies correspond to those of the $HE_{1,4}$ and $HE_{2,4}$ modes of an isolated tube with the same thickness variation, showing that the peaks are due to the red shift of the CLM cut-off frequencies.

In case of $\alpha = -0.1$, Fig. 12(b) compares points 5 and 6 at $F_\gamma = 2.208$, showing that the loss enhancement is more than four orders of magnitude. Fig. 12(d) shows that the enhancement is due to the hybridization of the FM with a CLM having a relatively quick azimuthal variation. For point 6, the chosen frequencies correspond to the cut-off of the single tube $EH_{5,3}$ mode, and the field profile highlighted in the inset of Fig. 12 corresponds to the $EH_{5,3}$ one, shown in the inset of Fig. 9. The same for points 7 and 8. Here the chosen frequency $F_\delta = 2.342$ corresponds to $EH_{10,3}$ and again the agreement between the field profiles is very good.

Mode hybridization and the deformation of the FM main lobe showed in Fig. 12(c) and (d) are also responsible of the A_{eff} changes showed in Fig. 4.

The comparison of the results shows a strong consistency between the model predictions using the single tube approximation and the numerical simulation of the whole fiber.

In order to have quantitative comparison and a global view of the effects, Fig. 13 shows for different α and in a single graph the second-order TB NCL spectra of #1 on one hand and the single tube CLMs $EH_{5,3}$, $EH_{10,3}$, $EH_{16,3}$, $EH_{25,3}$ (see Fig. 9) cut-off frequencies and $|g|^2$ (symbols and bar charts, respectively) on the other hand. Despite the limited number of CLMs used to illustrate the link between their F_c and $|g|^2$ and the NCL, the figure clearly highlights the good fit between the variation of NCL and the $|g|^2$ evolution when α changes, coherently with the model developed in Melli et al. (2024). The observed blue-shift in NCL's TB in the case of tube thinning is dominated by the $|g|^2$ increase of the low azimuthal index CLMs as illustrated with the $EH_{5,3}$, $EH_{10,3}$, and $EH_{16,3}$ modes. Here, these modes' $|g|^2$ value and F_c follow the NCL curves of the different fibers remarkably well. It also shows the variation of F_c induced by the thinning has a marginal impact of the NCL increase. Tube thickening does not cause a significant NCL variation, but only a decrease of the resonance frequencies. Finally, the discrepancy between the evolution of NCL and $EH_{25,3}$ $|g|^2$ is due to the resonance appearing at $F = 2.77$, caused by the F_c red-shift of modes $HE_{1,4}$ and $TE_{0,4}$.

5. Dependence on fiber's parameters

In this section, we attempt to address the following question: "what are the driving parameters in NCL alteration upon the considered tube thickening and thinning?". Before proceeding toward this goal, it is appropriate to summarize the main results of the analysis carried out so far. The loss enhancement affecting the perturbed fibers is due to the change in the coupling between FM and CLMs and it occurs at the cut-off frequencies of the latter. In case of thickening, the red shift of the cut-off frequencies of the CLMs and in particular of the low azimuthal index ones dominates with respect to the field distribution distortion. In this case, it is a matter of whether and which parameters affect the cut-off frequencies of the low azimuthal index CLMs. In case of thinning, the field distribution distortion dominates and in particular the consequent enhancement of the ASO causes the blue-shift of the blue-edge HLRs. In this case, the CLMs involved have an azimuthal index higher than the previous case and the question is addressed to whether and what parameters affect the cut-off frequencies of high azimuthal index CLMs. In summary, the distribution of the CLM cut-off normalized frequencies plays a decisive role in defining how the fiber physical and geometrical parameters affect the fibers sensitivity toward such kind of perturbations. This distribution depends on the tube shape ratio $\rho = 1 - t/r_{ext}$ and the dielectric refractive index n_d (Kharadly and Lewis, 1969), and thus simultaneously on several geometrical and physical fibers' parameters. This is the reason why the parameters of the fibers of Table 1 have been chosen to have different ρ and n_d values in the range of practical interest. An in-depth analysis of CLMs cut-off dependencies can be found in Vincetti and Setti (2010) and Vincetti and Rosa (2019), and their influences on TLF confinement loss is analyzed in Melli et al. (2024).

CLMs with low azimuthal index and radial index ν have cut-off frequencies very close to $F = \nu - 1$ and they are *de facto* independent of ρ and n_d. As a consequence, the red shift of the red-edges does not depend on fibers parameters. This is confirmed by Fig. 14, where the loss variation $\Delta NCL = NCL - NCL_0$ between perturbed fiber (NCL)

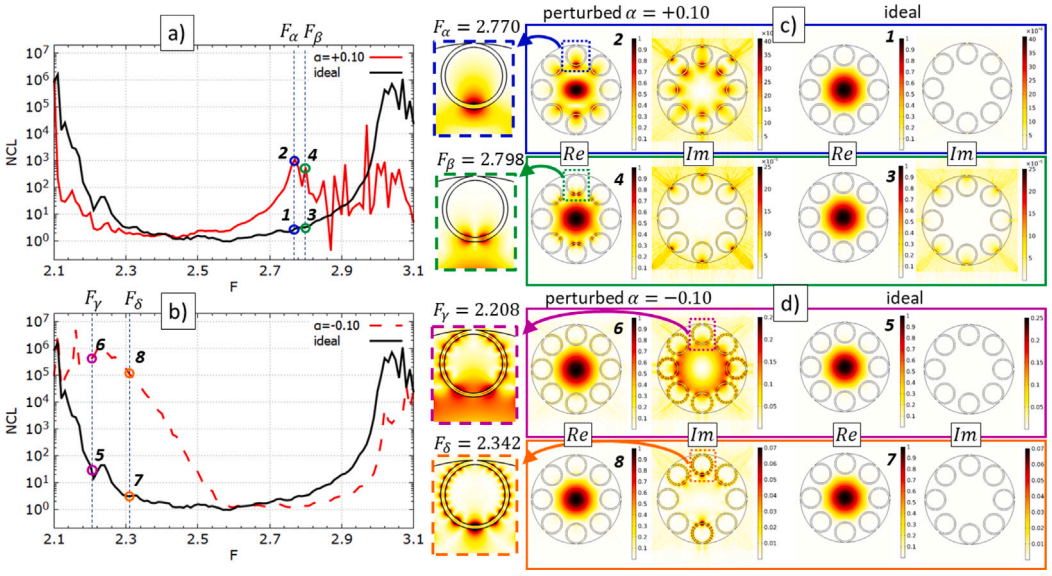

Fig. 12. Left: Detail of #1 NCL spectra between $F = 2.1$ and $F = 3.1$ in case of ideal and perturbed tubes with (a) $\alpha = +0.1$ and (b) $\alpha = -0.1$. Right: comparison of the electric field transverse component $\overline{E}_t$ real and imaginary parts for the perturbed and ideal fibers (left and right of each box, respectively) at the frequencies highlighted in the left panel with (c) $\alpha = +0.1$, and (d) $\alpha = -0.1$. All magnitudes are normalized to the corresponding real part maximum of the ideal fiber. Details of the field distribution in the tubes bounded by the dashed rectangles are show in the insets. (For interpretation of the references to color in this figure legend, the reader is referred to the web version of this article.)

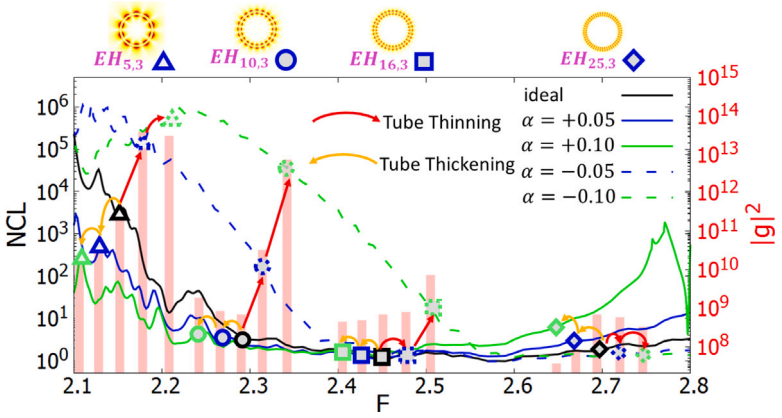

Fig. 13. CL spectra of #1 with ideal tubes ($\alpha = 0$, black), thicker tubes ($\alpha > 0$, solid colored), and thinner tubes ($\alpha < 0$, dashed colored). Symbols show NCL at F_c for $EH_{5,3}$ (triangles), $EH_{10,3}$ (circles), $EH_{16,3}$ (squares), and $EH_{25,3}$ (diamonds) CLMs. Orange and red arrows show CL variations caused by thickening and thinning the tubes, respectively. Red bars show the corresponding $|g|^2$ values. (For interpretation of the references to color in this figure legend, the reader is referred to the web version of this article.)

and ideal one (NCL_0) computed at $F = 2.7$ for $\alpha = +0.1$ is shown for all fibers here investigated. ΔNCL is substantially independent of ρ and n_d.

By increasing the azimuthal index, F_c progressively increases at a rate proportional to ρ and inversely proportional to n_d, so the higher the azimuthal index, the higher the dependence on ρ and n_d. The blue shift of the blue-edges occurring for tube thinning depends on the cut-off frequencies of CLMs with relatively high azimuthal index and thus depend on ρ and n_d. These features are shown in Fig. 14, where the loss variation ΔNCL computed at $F = 2.5$ for $\alpha = -0.1$ only depends on ρ and n_d irrespective of thickness, core size, number, and radius of the tubes of the fibers here investigated. By referring to Figs. 5 and 14, #1, #3, and #5 have the same blue shift because ρ and n_d are the same, even though t, R_{co}, r_{ext}, and N are different. The same is observed for fibers #4 and #6, even though they have a wider shift when compared to the first set, because their refractive index is higher. Fiber#2 has at least one parameter equal to the previous fibers, but having higher ρ and smaller or equal n_d, shows a smaller shift and ΔNCL.

The effects of the tube variation also depend on the radial index ν and consequently on the TB considered. In case of thickening, Fig. 7(b) shows that for low azimuthal index CLM the F_c shift increases with the radial index, explaining the increasingly red-shift of the peaks in CL spectra by increasing the TB order shown in Figs. 2(a), 3(a), and 5. In case of thinning, Fig. 11 shows the azimuthal spectrum broadening increases with ν making more higher the CL enhancement, as shown in Figs. 2(b), 3(c) and (d), and 5. Finally, the number of tubes does not significantly affect the high-loss edge shifts because, in the context of the single tube approximation, the features of the CLMs do not depend on the number of tubes.

In summary, fibers with the same CLM cut-off distributions (same ρ and n_d) exhibit the same loss variations. To make TLFs more resistant to the damaging effects of tube thickness variations, it is necessary to design them to work in the fundamental or low order TBs by keeping ρ as high as possible and preferably choosing materials with n_d as low as possible, since this allows the fiber to work in those TBs at the wavelengths of interest. Finally, a low number of tubes helps to increase the tube radius and thus ρ without increasing the core size.

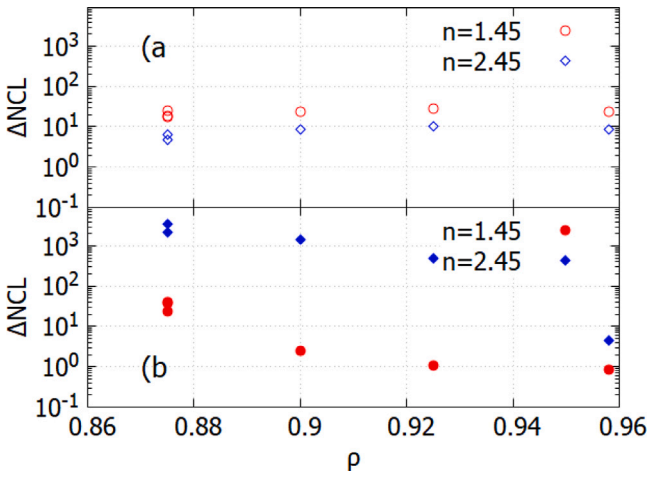

Fig. 14. Relative CL variation $\Delta NCL = NCL - NCL_0$ vs. ρ for the TLFs described in Table 1, computed at (a) $F = 2.7$ and $\alpha = +0.1$ and at (b) $F = 2.5$ and $\alpha = -0.1$. (For interpretation of the references to color in this figure legend, the reader is referred to the web version of this article.)

6. Conclusion

In this work, the effects of tube deformation in terms of thickness variation have been investigated and their detrimental effects on TLF performance in terms of confinement loss have been analyzed. Results show that tube thinning causes a frequency blue shift affecting the blue-edges of HLRs, and that tube thickening causes the appearance of red-shifted loss peaks. Both effects cause an increase of the loss in the TLF transmission bands and a reduction of their bandwidth. A study based on the inhibition of the coupling between FM and CLMs, single tube approximations and the Azimuthal Fourier Decomposition of the modes has been applied in order to understand and explain the mechanisms, and foresee the effects. The effectiveness of the approach is confirmed by numerical simulations. The study shows that the additional loss caused by the thickening is related to a red-shift of the low azimuthal index CLMs cut-off frequencies. The mechanism occurring in case of tube thinning is different. In that case, the deformations cause a modification of the field spatial distribution of the CLMs, which results in an increase of the coupling between FM and CLMs. Since in case of tube thinning the additional losses are related to the spectral distribution of the cut-off frequencies of the CLMs, any parameter affecting them plays a role in the additional loss. In particular, the increase of the ρ parameter or the reduction of the tube refractive index tend to increase the azimuthal index of the CLMs with cut-off frequency falling in the TBs, making the fibers more resilient toward tube thinning. An increase of the resilience both for thickening and thinning is also observed by reducing the order of the working TB. Although not all the possible disturbances have been included in the analysis here presented, the approach followed is quite general and can be applied to other kinds of analysis. Finally, it also shows the effectiveness of the IC model in describing the waveguiding mechanism of TLFs and the role played by the articulated set of CLMs.

CRediT authorship contribution statement

Federico Melli: Writing – original draft, Visualization, Methodology, Investigation, Data curation. **Fabio Giovanardi:** Methodology, Investigation, Data curation. **Kostiantyn Vasko:** Visualization, Methodology, Investigation, Data curation. **Lorenzo Rosa:** Writing – review & editing, Writing – original draft, Validation, Formal analysis, Data curation. **Fetah Benabid:** Writing – review & editing, Writing – original draft, Validation, Supervision, Formal analysis, Conceptualization. **Luca Vincetti:** Writing – review & editing, Writing – original draft, Validation, Formal analysis, Conceptualization.

Declaration of competing interest

The authors declare that they have no known competing financial interests or personal relationships that could have appeared to influence the work reported in this paper.

Data availability

Data will be made available on request.

Acknowledgments

This work is supported by the University of Modena and Reggio Emilia FAR DIP 2021 project SOQUANTS, Italy, Grant No. 554.2022, and H2020-FETOPEN-2018-2020 project CRYST[3], Grant No. 964531. F.M. acknowledges the European Commission for support through a grant in the context of H2020 project CRYST[3].

References

Amrani, Foued, Osório, Jonas H., Delahaye, Frédéric, Giovanardi, Fabio, Vincetti, Luca, Debord, Benoît, Gérôme, Frédéric, Benabid, Fetah, 2021. Low-loss single-mode hybrid-lattice hollow-core photonic-crystal fibre. Light Sci. Appl. 10 (1), 7. http://dx.doi.org/10.1038/s41377-020-00457-7.

Barozzi, Matteo, Manicardi, Alex, Vannucci, Armando, Candiani, Alessandro, Sozzi, Michele, Konstantaki, Maria, Pissadakis, Stavros, Corradini, Roberto, Selleri, Stefano, Cucinotta, Annamaria, 2017. Optical fiber sensors for label-free DNA detection. J. Lightwave Technol. 35 (16), 3461–3472. http://dx.doi.org/10.1109/JLT.2016.2607024.

Benabid, F., Roberts, P.J., 2011. Linear and nonlinear optical properties of hollow core photonic crystal fiber. J. Modern Opt. 58 (2), 87–124. http://dx.doi.org/10.1080/09500340.2010.543706.

Bradley, T.D., Jouin, J., McFerran, J.J., Thomas, P., Gerome, F., Benabid, F., 2014. Extended duration of rubidium vapor in aluminosilicate ceramic coated hypocycloidal core kagome HC-PCF. J. Lightwave Technol. 32 (14), 2486–2491.

Carcreff, Julie, Cheviré, Francois, Galdo, Elodie, Lebullenger, Ronan, Gautier, Antoine, Adam, Jean Luc, Coq, David Le, Brilland, Laurent, Chahal, Radwan, Renversez, Gilles, Troles, Johann, 2021. Mid-infrared hollow core fiber drawn from a 3D printed chalcogenide glass preform. Opt. Mater. Express 11 (1), 198–209. http://dx.doi.org/10.1364/OME.415090, OSA.

Couny, F., Benabid, F., Roberts, P.J., Light, P.S., Raymer, M.G., 2007. Generation and photonic guidance of multi-octave optical-frequency combs. Science 318 (5853), 1118–1121. http://dx.doi.org/10.1126/science.1149091.

Cruz, A.L.S., Franco, M.A.R., Cordeiro, C.M.B., Rodrigues, G.S., Osório, J.H., da Silva, L.E., 2017. Exploring THz hollow-core fiber designs manufactured by 3D printing. In: 2017 SBMO/IEEE MTT-S International Microwave and Optoelectronics Conference. IMOC, pp. 1–5. http://dx.doi.org/10.1109/IMOC.2017.8121109.

Debord, Benoît, Amrani, Foued, Vincetti, Luca, Gérôme, Frédéric, Benabid, Fetah, 2019. Hollow-core fiber technology: The rising of gas photonics. Fibers 7 (2), 16. http://dx.doi.org/10.3390/fib7020016.

Debord, B., Amsanpally, A., Alharbi, M., Vincetti, L., Blondy, J., Gérôme, F., Benabid, F., 2015. Ultra-large core size hypocycloid-shape inhibited coupling Kagome fibers for high-energy laser beam handling. J. Lightwave Technol. 33 (17), 3630–3634. http://dx.doi.org/10.1109/JLT.2015.2448794.

Debord, B., Amsanpally, A., Chafer, M., Baz, A., Maurel, M., Blondy, J.M., Hugonnot, E., Scol, F., Vincetti, L., Gérôme, F., Benabid, F., 2017. Ultralow transmission loss in inhibited-coupling guiding hollow fibers. Optica 4 (2), 209–217. http://dx.doi.org/10.1364/OPTICA.4.000209.

Gao, Shou-Fei, Wang, Ying-Ying, Ding, Wei, Hong, Yi-Feng, Wang, Pu, 2019. Hollow-Core Conjoined-Tube Negative-Curvature Fiber with Loss Approaching Rayleigh Scattering Limit of Silica, Conference on Lasers and Electro-Optics. Vol. STh1L.6, Optica Publishing Group, http://dx.doi.org/10.1364/CLEO_SI.2019.STh1L.6, Abstract: We report on a hollow-core conjoined-tube negative-curvature fiber with measured transmission losses of 2.7 dB/km at 1150 nm and 3.8 dB/km at 680 nm. The loss from 653 to 706 nm approaches the Rayleigh scattering limit of silica fiber.

Joseph Weiblen, R., Menyuk, Curtis R., Gattass, Rafael R., Brandon Shaw, L., Sanghera, Jasbinder S., 2016. Fabrication tolerances in As2S3 negative-curvature antiresonant fibers. Opt. Lett. 41 (11), 2624–2627. http://dx.doi.org/10.1364/OL.41.002624, OSA.

Kharadly, M.M.Z., Lewis, J.E., 1969. Properties of dielectric-tube waveguides. Proc. IEE 116 (2), 214–224. http://dx.doi.org/10.1049/piee.1969.0045.

Khozeymeh, Foroogh, Melli, Federico, Capodaglio, Sabrina, Corradini, Roberto, Benabid, Fetah, Vincetti, Luca, Cucinotta, Annamaria, 2022. Hollow-core fiber-based biosensor: A platform for lab-in-fiber optical biosensors for DNA detection. Sensors 22 (14), 5144. http://dx.doi.org/10.3390/s22145144.

Knight, J.C., Birks, T.A., Russell, P.St.J., Atkin, D.M., 1996. All-silica single-mode optical fiber with photonic crystal cladding. Opt. Lett. 21, 1547–1549.

Melli, F., Giovanardi, F., Rosa, L., Benabid, F., Vincetti, L., 2021. Analysis and assessment of tube thickness variation effect in hollow-core inhibited coupling tube lattice fibers. In: 2021 Conference on Lasers and Electro-Optics Europe and European Quantum Electronics Conference. Optica Publishing Group, p. ce_p_2.

Melli, Federico, Vasko, Kostiantyn, Rosa, Lorenzo, Benabid, Fetah, Vincetti, Luca, 2024. Azimuthal Fourier decomposition for loss analysis of hollow-core tube lattice fibers part I: Ideal fibers. Results Opt. (ISSN: 2666-9501) 15, 100657. http://dx.doi.org/10.1016/j.rio.2024.100657.

Osório, Jonas H., Chafer, Matthieu, Debord, Benoît, Giovanardi, Fabio, Cordier, Martin, Maurel, Martin, Delahaye, Frédéric, Amrani, Foued, Vincetti, Luca, Gérôme, Frédéric, Benabid, Fetah, 2019. Tailoring modal properties of inhibited-coupling guiding fibers by cladding modification. Sci. Rep. 9, 1376. http://dx.doi.org/10.1038/s41598-018-37948-y, Nature.

Pryamikov, Andrey D., Biriukov, Alexander S., Kosolapov, Alexey F., Plotnichenko, Victor G., Semjonov, Sergei L., Dianov, Evgeny M., 2011. Demonstration of a waveguide regime for a silica hollow-core microstructured optical fiber with a negative curvature of the core boundary in the spectral region > 3.5 μm. Opt. Express 19 (2), 1441–1448. http://dx.doi.org/10.1364/OE.19.001441.

Roberts, P.J., Couny, F., Sabert, H., Mangan, B.J., Williams, D.P., Farr, L., Mason, M.W., Tomlinson, A., Birks, T.A., Knight, J.C., St.J. Russell, P., 2005. Ultimate low loss of hollow-core photonic crystal fibres. Opt. Express 13 (1), 236–244. http://dx.doi.org/10.1364/OPEX.13.000236, OSA.

Rosa, Lorenzo, Melli, Federico, Vincetti, Luca, 2021. Analytical formulas for dispersion and effective area in hollow-core tube lattice fibers. Fibers 9 (10), http://dx.doi.org/10.3390/fib9100058.

Sakr, H., Chen, Y., Jasion, T.G., Bradley, T., Hayes, J.R., Mulvad, H.C.H., Davidson, I.A., Numkam Fokoua, E., Poletti, F., 2020. Hollow core optical fibres with comparable attenuation to silica fibres between 600 and 1100 nm. Nature Commun. 11, http://dx.doi.org/10.1038/s41467-020-16106-9.

Sakr, H., Jasion, G.T., Bradley, T.D., Chen, Y., Hayes, J.R., Davidson, I.A., Mulvad, H.-C., Xu, L., Richardson, D.J., Poletti, F., 2019. Record low loss hollow core fiber for the 1 μm region. In: 2019 Conference on Lasers and Electro-Optics Europe and European Quantum Electronics Conference. Optica Publishing Group, p. ce_5_5. http://dx.doi.org/10.1364/CLEO_EUROPE.2019.ce_5_5.

Shi, Chao, Lu, Chao, Gu, Claire, Tian, Lei, Newhouse, Rebecca, Chen, Shaowei, Zhang, Jin Z., 2008. Inner wall coated hollow core waveguide sensor based on double substrate surface enhanced Raman scattering. Appl. Phys. Lett. 93 (15), 153101.

Ventura, Andrea, Hayashi, Juliano Grigoleto, Cimek, Jaroslaw, Jasion, Gregory, Janicek, Petr, Slimen, Fedia Ben, White, Nicholas, Fu, Qiang, Xu, Lin, Sakr, Hesham, Wheeler, Natalie V., Richardson, David J., Poletti, Francesco, 2020. Extruded tellurite antiresonant hollow core fiber for Mid-IR operation. Opt. Express 28 (11), 16542–16553. http://dx.doi.org/10.1364/OE.390517.

Vincetti, Luca, 2016. Empirical formulas for calculating loss in hollow core tube lattice fibers. Opt. Express 24 (10), 10313–10325. http://dx.doi.org/10.1364/OE.24.010313, OSA.

Vincetti, Luca, Rosa, Lorenzo, 2019. A simple analytical model for confinement loss estimation in hollow-core tube lattice fibers. Opt. Express 27 (4), 5230–5237. http://dx.doi.org/10.1364/OE.27.005230.

Vincetti, Luca, Setti, Valerio, 2010. Waveguiding mechanism in tube lattice fibers. Opt. Express 18 (22), 23133–23146. http://dx.doi.org/10.1364/OE.18.023133.

Zheng, Ximeng, 2017. Fiber Post-Processing and Atomic Spectroscopy for the Development of Atomic-Vapour Photonic Microcell (Ph.D. thesis). University of Limoges.